University of Toronto

Department of Physics

M.Sc. Option I Report

Modeling Internal Wave and Energy Propagation through Stratified Fluids using a Spectrally-Based DNS

Author
M.G. Schee

Supervisor
Prof. Nicolas Grisouard

August 23, 2019

Abstract

A direct numerical simulation (DNS) is adapted to solve the Boussinesq equations of motion using spectral methods. The DNS is used to reproduce the results of laboratory experiments by Ghaemsaidi et al. (2016) showing the transmission and reflection of internal waves from mixed layers in a vertically stratified fluid. The DNS is used to analyze the vertical energy flux through several different vertical stratification profiles. This work shows potential of being used to analyze the vertical propagation of internal wave energy through stratification profiles similar to those found in the Arctic Ocean.

1 Introduction

The North Atlantic Current sends relatively warm and salty water into the Arctic Ocean (Carmack et al., 1997; Wells and Wettlaufer, 2007). In most parts of the ocean, water is less dense when warm than when cold, but the Arctic is cold enough so differences in temperature and salinity both have a significant effect on density. Such waters are called beta oceans to distinguish from the alpha oceans found in the tropics and mid-latitudes (Carmack, 2007).

Water sent poleward from the Atlantic forms the Warm Atlantic Layer (WAL) as it subducts under the less dense surface waters which enter the Arctic Ocean from rivers. The WAL is centered around a depth of 300-500 m, just below the pycnocline where density increases rapidly with depth (Wells and Wettlaufer, 2007). In the pycnocline, the strong stratification is accompanied by layers on the order of 1 m thick having well defined and homogenous temperature and salinity separated by sharp gradient interfaces (Sutherland, 2016; Shibley and Timmermans, 2019). These characteristic vertical stratification structures, seen in Figure 1, are called double-diffusive staircases. Both the staircases and the WAL are persistent and wide-spread features of the Arctic Ocean (Carmack et al., 1997; Shibley and Timmermans, 2019).

Turner (2010) calculated that the WAL contains enough heat to completely melt the Arctic sea ice cover within four years if allowed to rise to the surface. The strong stratification of the pycnocline prevents the majority of heat transport up from the WAL which is why sea ice can form over the Arctic Ocean's basins (Fer, 2014; Carmack, 2007).

Arctic ice cover limits the energy transferred to the ocean from wind-driven shear and increases the dissipation of internal waves (Fer, 2014). Sea ice in the Arctic has been declining for decades (Comiso et al., 2008) and exposing more of the ocean's surface can

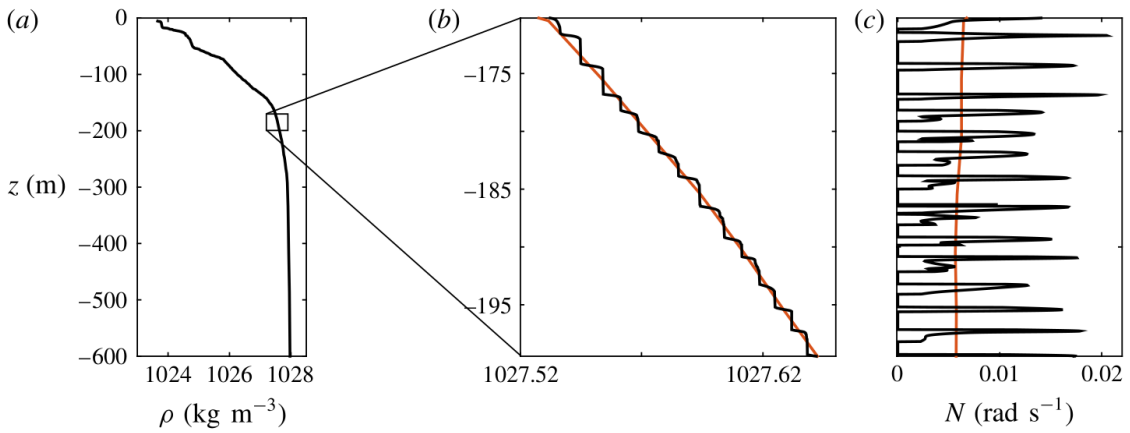

Figure 1: (a) A typical density stratification profile in the Canadian Basin of the Arctic Ocean (Rainville and Winsor, 2008). (b) A magnified section of the profile showing the staircase structure. The red line is a 5 m bin-averaged smoothed density profile. (c) The corresponding profile for the buoyancy frequency $N(z)$. Reproduced from Figure 1 of Ghaemsaidi et al. (2016).

lead to more wind-generated internal waves propagating deeper, causing vertical mixing (Fer, 2014; Rainville et al., 2011).

As vertical mixing increases, heat from the WAL will more easily be transferred to the surface leading to further ice loss which will allow more wind energy to transfer into the ocean in a positive feedback loop (Turner, 2010). The continued loss of sea ice in the Arctic will have major consequences for both the resident ecosystems and large scale circulation (Comiso et al., 2008; Ghaemsaidi et al., 2016).

There is a body of previous work on the interactions between internal waves and double-diffusive staircases, but it is still unclear to what extent internal waves can penetrate such stratification structures (Sutherland, 2016). In section 2 of this report, I adapt a direct numerical simulation (DNS) using the Dedalus framework to model the propagation of internal waves generated at the surface through a density stratified fluid. In section 3, I use the DNS to reproduce the results of a laboratory experiment by Ghaemsaidi et al. (2016) involving internal waves being sent through a fluid with one or two mixed layers. I extend the DNS in section 4 to analyze the vertical energy flux through the single layer, double layer, and constant stratification profiles. In section 5, I suggest extensions to this project which could bring it closer to simulating internal wave and energy propagation in the Arctic Ocean.

2 Methods

2.1 The Boussinesq Equations of Motion

The code for this work uses the Dedalus framework for solving partial differential equations (Burns et al., 2019). I choose to adapt an example simulation run in two dimensions to reduce the required computing time and memory resources. Because Coriolis effects were not present in the laboratory experiment from Ghaemsaidi et al. (2016) and they are not essential to the dynamics of interest, I choose to neglect rotation. This DNS is centered around solving the Boussinesq equations of motion for a vertically density-stratified, non-rotating, nearly incompressible fluid in two dimensions:

$$\nabla \cdot \vec{v} = 0 \tag{1a}$$

$$\frac{Db}{Dt} = \kappa \nabla^2 b - N^2(z) w \tag{1b}$$

$$\frac{D\vec{v}}{Dt} = \nu \nabla^2 \vec{v} - \nabla p' + b\hat{z} \tag{1c}$$

where $\vec{v} = (u, w)$ is velocity vector, κ is molecular diffusivity, and ν is molecular viscosity. The Boussinesq approximation considers density variations to be negligible unless they effect buoyancy forces because g is relatively large (Vallis, 2017; Sutherland, 2010). This is a reasonable approximation for the ocean because density variations are small (Sutherland, 2010).

Equation (1a) is the continuity equation and states that the flow is non-divergent (Lautrup, 2011). Equation (1b) is the equation of state, which is usually written in terms of density or temperature (Winters et al., 2004; Lautrup, 2011). For a more convenient form in terms of buoyancy, I define the total density to be

$$\rho(\vec{x}, t) = \rho_0 + \overline{\rho}(z) + \delta\rho(\vec{x}, t) \tag{2}$$

where ρ_0 is a constant reference density, $\overline{\rho}$ is the background density profile, and $\delta\rho$ represents density fluctuations, which I consider to be small for this work (Vallis, 2017).

Similarly, I define the total pressure as

$$p(\vec{x}, t) = p_0 + \overline{p}(z) + \delta p(\vec{x}, t) \tag{3}$$

where I set the background pressure $p_0 + \overline{p}(z)$ in hydrostatic balance with ρ_0. Then I define $b = -g\delta\rho/\rho_0$ as the buoyancy (Vallis, 2017) and the background stratification frequency $N(z)$ as

$$N^2(z) = -\frac{g}{\rho_0}\frac{\partial \overline{\rho}}{\partial z}. \tag{4}$$

Equation (1c) is the momentum equation where I define $p' = \delta p/\rho_0$ as the normalized pressure variations.

2.2 Dedalus Code

2.2.1 Domain and Bases

Dedalus is a framework built to use spectral methods to solve arbitrary systems of differential equations (Burns et al., 2019). It is primarily designed to study problems in fluid dynamics and can be run in parallel using MPI. I choose to adapt an example from the Dedalus development team which used similar equations in two dimensions. Because I am primarily interested in vertical motion, I use a Chebyshev basis in the z direction. This allows me to define non-constant coefficients (NCC's), such as the background stratification $N(z)$. For the horizontal direction, I use a Fourier basis which implicitly defines periodic boundary conditions in x. For simplicity, I set the initial conditions of all the variables to zero and use a two-stage, second-order, diagonally implicit Runga-Kutta time stepping scheme with a constant $dt = 0.125$ seconds (Ascher et al., 1997).

Ideally, my domain would extend infinitely downward in z. Being limited to a finite length, the downward propagating waves reflect off the bottom boundary and propagate upwards, creating interference. To mitigate this issue, I extend the vertical simulation domain below where I am taking measurements. Because I am not interested in the flow below that point, this extra buffer has a lower resolution.

2.2.2 Boundary Conditions and Forcing

My problem contains three state variables; b, u, and w, which appear in first order time derivatives, and one diagnostic variable; p'. I set periodic boundary conditions in the x direction by using a Fourier basis and specify six Dirichlet boundary conditions in the z direction. For the first three, I set the state variables equal to zero at the bottom of the domain. At the top of the domain (z_{top}), I prescribe functions for the boundary conditions on b, u, and w to force downward-propagating internal waves.

A polarization relation between the state variables can be found by linearizing the equations of motion and seeking wave solutions in the form

$$\exp\left[i(k_x x + k_z z - \omega t)\right] \tag{5}$$

where k_x and k_z are the horizontal and vertical wavenumbers and ω is the frequency of the boundary forcing (Cushman-Roisin and Beckers, 2011). By assuming the coefficient for the buoyancy wave solution to be $\hat{A}g$, the polarization relation is

$$u = -\hat{A}\frac{g\omega k_z}{N^2 k_x}\sin\left(k_x x + k_z z - \omega t\right) \tag{6a}$$

$$w = +\hat{A}\frac{g\omega}{N^2}\sin\left(k_x x + k_z z - \omega t\right) \tag{6b}$$

$$p' = -\hat{A}\frac{g\omega^2 k_z}{N^2 k_x^2}\sin\left(k_x x + k_z z - \omega t\right) \tag{6c}$$

$$b = +\hat{A}g\cos\left(k_x x + k_z z - \omega t\right) \tag{6d}$$

where $\hat{A}$ is a non-dimensional forcing amplitude coefficient, which is taken to be small for this work (Cushman-Roisin and Beckers, 2011).

Because I set the initial conditions of all variables to zero, using (6) directly as the top boundary forcing causes a transient oscillation that eventually dies out. To avoid this transient, I apply a temporal ramp function

$$R_{bf}(t) = \frac{1}{2}\left(\tanh\left[\frac{4t}{nT} - 2\right] + 1\right) \tag{7}$$

to each forcing amplitude in (6). $T = 2\pi/\omega$ is the oscillation period and I set the ramp to last $n = 3$ oscillation periods because it is long enough to make the transient oscillation negligible but not long enough to make the simulation spin up time cumbersome.

2.2.3 Condition for Linearity

I am only interested in investigating linearly stable flows. Monitoring the Richardson number Ri is one method because if Ri$> 1/4$, then linear stability is guaranteed (Kundu et al., 2015). However, since Ri is proportional to N^2 and I set $N = 0$ explicitly in sections of the background profile, I choose to monitor a linear criterion C_{lin} that comes from the linearized horizontal momentum equation. Again assuming the form (5) for u and w, I find the condition for linearity to be when:

$$C_{lin} = \frac{k_x u + k_z w}{\omega} << 1 \tag{8}$$

is satisfied everywhere in the flow. For all simulations in this work, C_{lin} is on the order of 0.1 or smaller at all times.

2.3 Calculating Vertical Energy Flux

I am interested in finding the vertical energy flux through a horizontal surface at some depth z. The change in kinetic energy per unit mass is

$$\frac{\partial E_k}{\partial t} = \frac{1}{2}\frac{\partial |\vec{v}|^2}{\partial t}. \tag{9}$$

I derive an expression for $\partial E_k/\partial t$ by taking the dot product of the momentum equation (1c) with $\vec{v}$. After expanding the material derivative, this gives:

$$\frac{\partial E_k}{\partial t} = \vec{v} \cdot \frac{\partial \vec{v}}{\partial t} = -\vec{v} \cdot (\vec{v} \cdot \nabla)\vec{v} + \vec{v} \cdot \mathcal{D}\vec{v} - \vec{v} \cdot \nabla p' + \vec{v} \cdot b\hat{z} \tag{10}$$

where $\mathcal{D}$ is a dissipation operator in two dimensions

$$\mathcal{D} = \nu_x \frac{\partial^2}{\partial x^2} + \nu_z \frac{\partial^2}{\partial z^2} \tag{11}$$

where ν_x and ν_z are the horizontal and vertical kinematic viscosities, respectively.

The general procedure is to split each term into divergent and non-divergent terms. Using the product rule, the viscous term can be written as

$$\vec{v} \cdot \mathcal{D}\vec{v} = \nu_x \left[\frac{\partial^2 E_k}{\partial x^2} - \left(\frac{\partial \vec{v}}{\partial x} \right)^2 \right] + \nu_z \left[\frac{\partial^2 E_k}{\partial z^2} - \left(\frac{\partial \vec{v}}{\partial x} \right)^2 \right] \tag{12}$$

which can be simplified to

$$\vec{v} \cdot \mathcal{D}\vec{v} = \nabla \cdot \vec{\phi}_\nu - \epsilon \tag{13}$$

by defining the viscous flux vector

$$\vec{\phi}_\nu = \nu_x \frac{\partial E_k}{\partial x} \hat{x} + \nu_z \frac{\partial E_k}{\partial z} \hat{z} \tag{14}$$

and the dissipation

$$\epsilon = \nu_x \left(\frac{\partial \vec{v}}{\partial x} \right)^2 + \nu_z \left(\frac{\partial \vec{v}}{\partial z} \right)^2. \tag{15}$$

Following a similar procedure for the other terms and using the fact that the flow is non-divergent, (10) can be written as

$$\frac{\partial E_k}{\partial t} = -\nabla \cdot \left((E_k + p')\vec{v} - \vec{\phi}_\nu \right) + bw - \epsilon. \tag{16}$$

From this I define the vertical energy flux

$$F_z = (E_k + P)\vec{v} \cdot \hat{z} - \vec{\phi}_\nu \cdot \hat{z} = (E_k + p')w - \nu_z \frac{\partial E_k}{\partial z} \tag{17}$$

where the sign of F_z is defined so a negative energy flux corresponds to energy propagating downwards. I choose a control volume that extends from the top boundary down to a depth of interest and across the full x extent from x_{min} to x_{max}. Integrating F_z along x gives

$$\int_{x_{min}}^{x_{max}} F_z dx = < F_z(z,t) > \tag{18}$$

the vertical energy flux per unit mass at a certain time (t) across a horizontal boundary at a certain depth (z).

Expanding E_k with (9) and $|\vec{v}|^2 = u^2 + w^2$ then using the product rule puts vertical energy flux in terms of u, w, p', and ν_z; values which are readily available in the code:

$$F_z = \frac{1}{2}(u^2 w + w^3) + p' w - \nu_z \left(u \frac{\partial u}{\partial z} + w \frac{\partial w}{\partial z} \right) \tag{19}$$

The three terms represent the vertical energy flux due to kinetic advection F_{KA}, pressure work F_{PW}, and viscosity F_{VIS}, respectively. The relative size of each term can be found by substituting the polarization relation (6):

$$F_{KA} = \left(\frac{\hat{A} g \omega}{N^2} \right)^3 \frac{1}{2} \left(\frac{k_z^2}{k_x^2} + 1 \right) \sin^3(k_x x + k_z z - \omega t) \tag{20a}$$

$$F_{PW} = -\left(\frac{\hat{A} g \omega}{N^2} \right)^2 \frac{\omega k_z}{k_x^2} \sin^2(k_x x + k_z z - \omega t) \tag{20b}$$

$$F_{VIS} = -\left(\frac{\hat{A} g \omega}{N^2} \right)^2 \nu_z k_z \left(\frac{k_z^2}{k_x^2} + 1 \right) \sin(k_x x + k_z z - \omega t) \cos(k_x x + k_z z - \omega t) \tag{20c}$$

The coefficient of pressure work is the largest in magnitude. Pressure work scales with $\hat{A}^2$ while kinetic advection scales with $\hat{A}^3$ and $\hat{A}$ is small. The viscous term will be small due to the small magnitude of the viscosity coefficient ν_z. When integrating over an integer number of horizontal wavelengths, the kinetic advection and viscous term will go to zero. Therefore, I expect the total vertical energy flux per unit mass to be entirely due to pressure work.

3 Validation with Experimental Results

3.1 Reproducing Experimental Conditions

Ghaemsaidi et al. (2016) performed a laboratory experiment to investigate the propagation of internal waves through vertical stratification. The tank they used was 0.54 m deep and 5.46 m long. However, the measurement domain was a 0.5 by 0.5 m area just to

the right of the wave generator which was a cylinder extending in the y direction that oscillated in z with an amplitude of 7 mm (Ghaemsaidi et al., 2016). The tank had parabolic ends to dissipate unwanted reflections from the boundaries. The domain I simulate is 1.5 by 1.5 m, but my measurement domain is centered in the horizontal and at the top of the vertical domain, with the remaining 1 m below as a buffer for unwanted reflections.

The two different stratification profiles used by Ghaemsaidi et al. (2016) both had constant stratifications of $N_1 = 0.95$ rad s^{-1} above and $N_2 = 1.24$ rad s^{-1} below the mixed layers. Between those two constant stratifications were either one or two mixed layers with $N = 0$. See Figure 2. I reproduce both the single and double layer profiles using combinations of tanh functions in order to keep the profiles smooth and continuous.

I use the same value of viscosity, $\nu = 10^{-6}$ m^{2}s^{-1}, as Ghaemsaidi et al. (2016) which is the viscosity of pure water at 20°C. The diffusivity (κ) used was not specified, so I use the corresponding value for pure water at 20°C: $\kappa = 1.4 \cdot 10^{-7}$ m^{2}s^{-1} (Kundu et al., 2015).

The oscillating frequencies used by Ghaemsaidi et al. (2016) in the scenarios I reproduce (see Figure 2) were not specified. Following Foran (2017), who successfully reproduced the simulation through a different means, I choose the frequencies $\omega = 0.67$ s^{-1} and $\omega = 0.72$ s^{-1} for the single and double mixed layer profiles, respectively.

Both Ghaemsaidi et al. (2016) and Foran (2017) used a characteristic total wavenumber of $k = 45$ m^{-1} for the boundary forcing. Through trigonometry and the dispersion relation of internal waves (Cushman-Roisin and Beckers, 2011):

$$\theta = \cos^{-1}(\omega/N_1), \qquad k_x = k\cos(\theta), \qquad k_z = k\sin(\theta) \tag{21}$$

this corresponds to an angle below the horizontal $\theta_1 = 45.1°$, $k_{x,1} = 31.7$ m^{-1}, and $k_{z,1} = 31.9$ m^{-1} for the single layer and $\theta_2 = 40.7°$, $k_{x,2} = 34.1$ m^{-1}, and $k_{z,2} = 29.4$ m^{-1} for the double layer.

To simulate the wave generator, I apply a windowing function

$$W_{bf}(x) = \frac{1}{4}\left(\tanh\left[s(x - x_l)\right] + 1\right)\left(\tanh\left[-s(x - x_r)\right] + 1\right) \tag{22}$$

to the top boundary forcing where s is the slope of the window's sides, x_l is the window's

left edge, and x_r is the window's right edge. I set $s = 20$ for a balance between edges too steep to run the code efficiently and edges too shallow to form well-defined wave beams. To have the waves originate from the top left corner of the display domain, I set $x_l = -\lambda_x/2$ and $x_r = \lambda_x/2$ where $\lambda_x = 2\pi/k_x$ is the horizontal wavelength.

Setting the parameters as stated and applying both the ramp (7) and windowing (22) to the top boundary forcing (6) creates an internal wave beam that propagates from the top left towards the bottom right of my 0.5 by 0.5 m measurement domain.

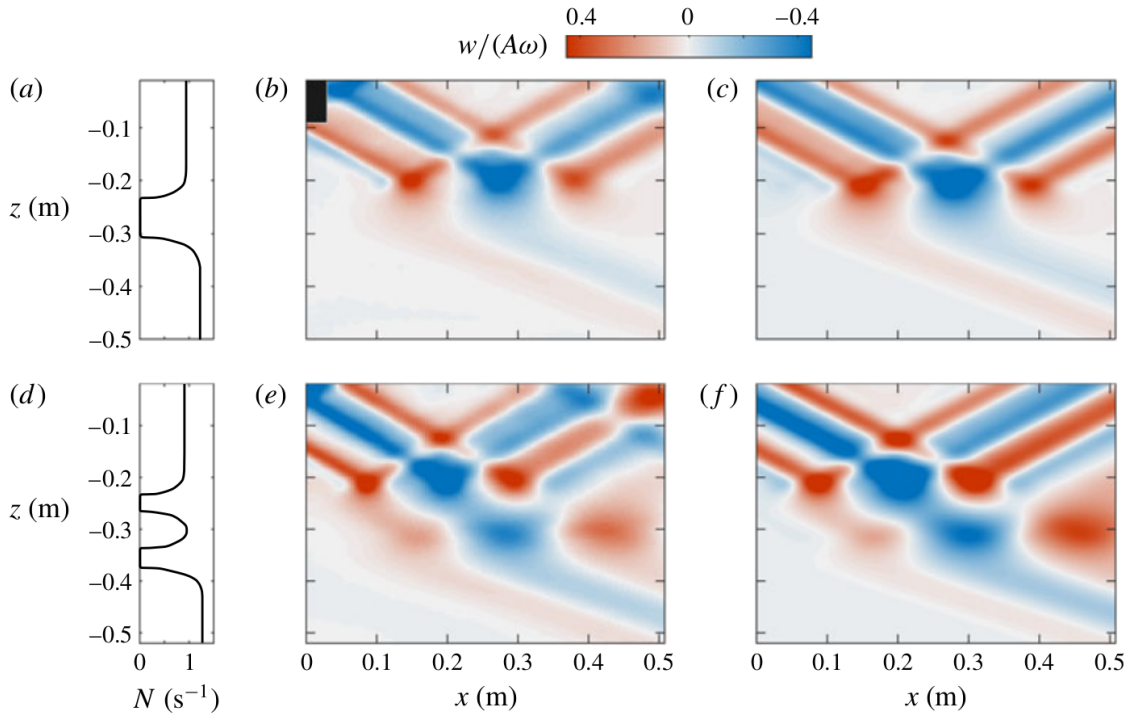

Figure 2: The results of the single (top row) and double (bottom row) mixed layer experiments run by Ghaemsaidi et al. (2016). (a,d) show the stratification profiles. (b,e) show vertical velocity snapshots from laboratory experiments. (c,f) show vertical velocity snapshots of theoretical wave fields. Reproduced from Figure 5 of Ghaemsaidi et al. (2016).

3.2 Comparison of Results

In both laboratory experiments and theoretical simulations, Ghaemsaidi et al. (2016) saw the majority of the wave beam reflect off the single layer and two distinct reflections and transmissions for the double layer. See Figure 2. All of the major features were successfully reproduced by Foran (2017) by recreating the stratification profiles as closely as possible and tuning ω until the correct angle was reached.

By following Foran (2017), I also successfully reproduce the major features of the experiments by Ghaemsaidi et al. (2016). In Figure 3, the wave beam mostly reflects off the single layer, with a small amount transmitted. In Figure 4, the wave beam has both reflection and transmission from both mixed layers.

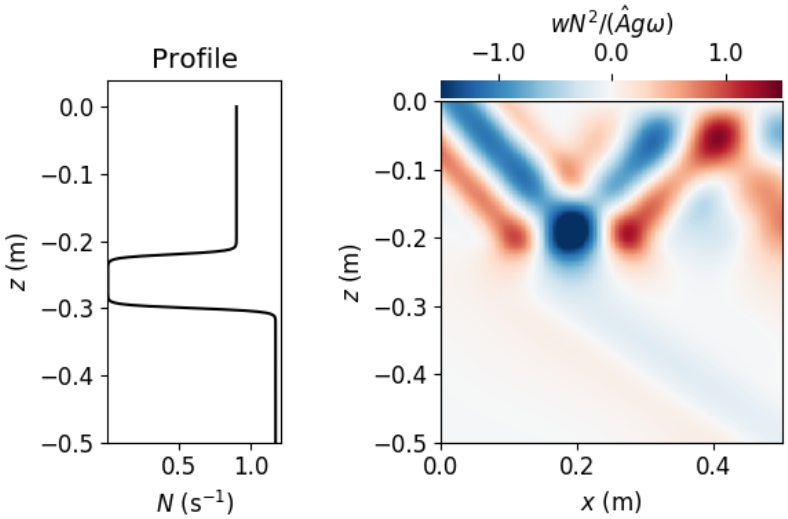

Figure 3: The stratification profile and a snapshot of the vertical velocity field for reproducing the single layer experiment. Compare to Figure 2 b,c. This simulation was run with $\omega = 0.67$ s^{-1}, $\hat{A} = 2.3 \cdot 10^{-4}$, and a resolution of 512×512. This snapshot was taken after 8.371 periods.

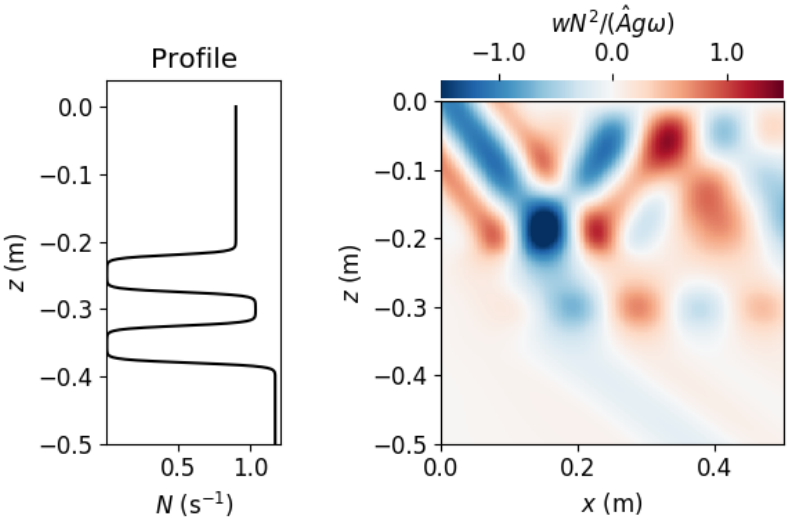

Figure 4: The stratification profile and a snapshot of the vertical velocity field for reproducing the single layer experiment. Compare to Figure 2 e,f. This simulation was run with $\omega = 0.72$ s^{-1}, $\hat{A} = 2.3 \cdot 10^{-4}$, and a resolution of 512×512. This snapshot was taken after 9.325 periods.

The magnitudes of the vertical velocity w differ between my results and those I am

reproducing due to different normalization methods. Ghaemsaidi et al. (2016) normalizes w by the "characteristic vertical velocity amplitude $A\omega$" where $A = 7.07$ mm is the amplitude and ω is the frequency of the wave-generating cylinder's oscillations. With no physical displacement distance, I choose to normalize w by the coefficient from (6b) the polarization relation for vertical velocity: $\hat{A}g\omega/N^2$.

The color bars for vertical velocity in Figures 3 and 4 are saturated to more clearly show the transmission of the wave beams. While it is expected that the transmission magnitude would be small, it is smaller still because of the relatively small value $\hat{A} = 2.3 \cdot 10^{-4}$. Amplitudes any larger cause aliasing which crash the solver.

4 Measuring Vertical Energy Flux

4.1 Energy Flux for a Constant Stratification Profile

To test the code's functionality to measure energy flux I use a profile with the constant stratification of $N = 1$ s^{-1} so the waves forced from the boundary can propagate freely through the domain. Therefore, I expect the vertical energy flux to be negative for all points in time and across all depths. Energy propagates vertically at the vertical group velocity

$$c_{gz} = \frac{\partial \omega}{\partial k_z} = -\frac{\omega k_z}{(k_x^2 + k_z^2)} \tag{23}$$

therefore I expect the energy flux to increase in magnitude at this rate for lower depths (Cushman-Roisin and Beckers, 2011).

For measuring vertical energy flux, having well defined wave beams is not important. This allows me to save on computational resources by removing the windowing function on the boundary forcing and setting the horizontal simulation domain from 0 to 0.5 m. To maintain a similar horizontal wavenumber to the above simulations and have an integer number of wavelengths across the top boundary, I set the boundary forcing wavelength equal to one third of the horizontal extent. I choose $\theta = 45°$ which results in $k_x = k_z = 37.7$ and $\omega = 0.707$ s^{-1}. With these parameters, I use (23) to predict a lag of approximately 6 oscillation periods between energy flux through the top and bottom boundaries.

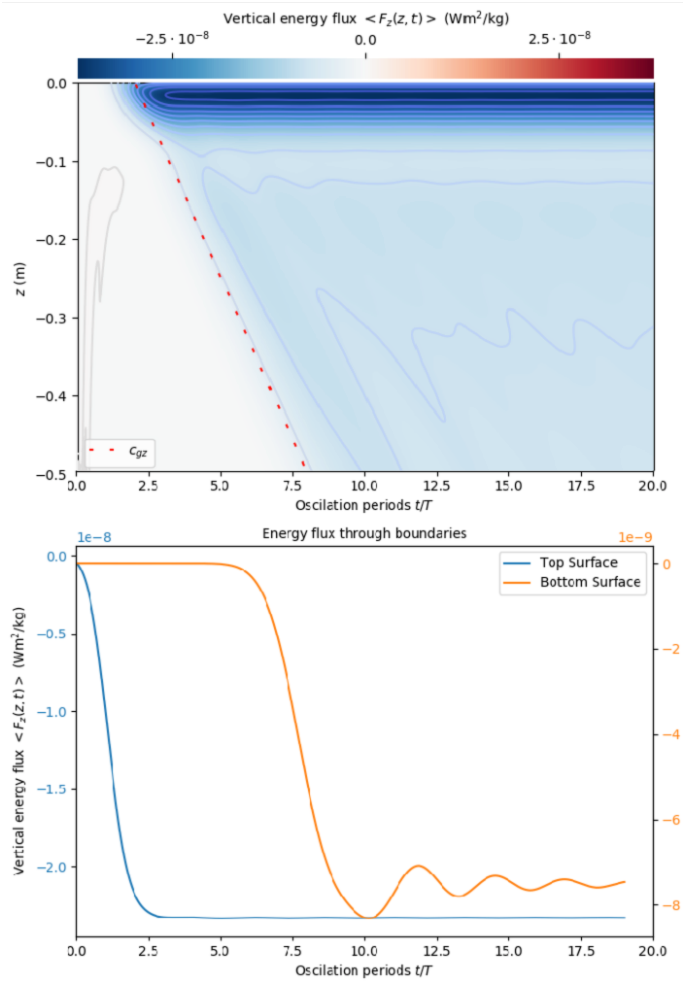

Figure 5: Energy flux for a constant stratification profile. The top panel shows the energy flux across the z domain and across time. The red dotted line shows the vertical group speed c_{gz}. The bottom panel shows the energy flux through the top boundary $z = 0$ and the bottom boundary $z = -0.5$ over time. This simulation had $\omega = 0.707$ s^{-1}, $\hat{A} = 2 \cdot 10^{-4}$ with a resolution of 512×512, and was run for 20 oscillation periods.

Figure 5 shows the vertical energy flux through constant stratification over 20 oscillation periods. In the top panel, the red dashed line shows a slope corresponding to c_{gz}. This line is offset horizontally to accentuate how closely it matches the propagation of energy. In the bottom panel, the lag between the top and bottom boundaries in energy flux is close to the predicted 6 periods.

The ramp in the forcing function is clearly evident in the energy flux through the top boundary. After approximately 3 periods, the top surface reaches a stead state. After a lag of around 6 periods, the ramp is also evident in the bottom boundary. While there is a small transient over the bottom boundary steady state, there is no evidence of interference

of waves reflected from the bottom of the buffer in the simulated domain after 20 periods.

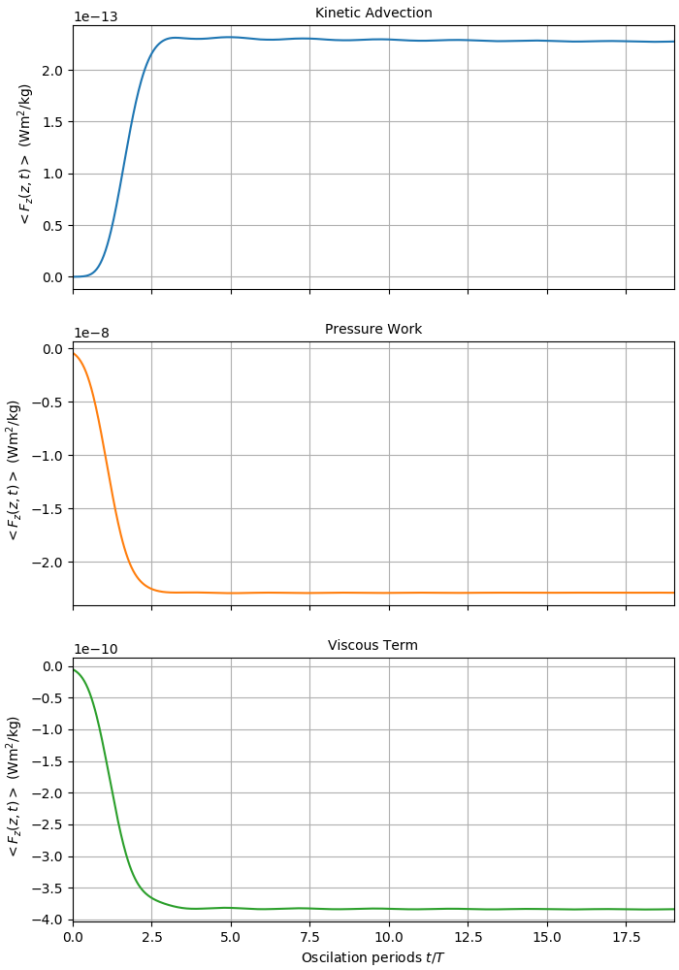

Figure 6: The 3 energy flux terms in (19) on the top boundary for a constant stratification profile: kinetic advection (top), pressure work (middle), and viscous term (bottom). Note the varying energy flux magnitudes between terms. This simulation had $\omega = 0.707$ s^{-1}, $\hat{A} = 2 \cdot 10^{-4}$ with a resolution of 512×512, and was run for 20 oscillation periods.

Figure 6 shows plots of the three energy flux terms from (20) integrated across the top boundary from the same simulation as Figure 5. Again, the ramp function over the first 3 periods is evident. Because the terms were integrated over 3 horizontal wavelengths λ_x, I expect the only non-zero term to be pressure work. Reaching a steady state value around $2.3 \cdot 10^{-13}$ Wm^2/kg, the kinetic advection is small enough to be arguably negligable but with a steady state value around $-3.8 \cdot 10^{-10}$ Wm^2/kg, the viscous term is definitely higher than expected. The pressure work reached a steady value around $-2.3 \cdot 10^{-8}$ Wm^2/kg. The value predicted by integrating (20b) from $x = 0$ to $x = 3\lambda_x$ is $-9.0 \cdot 10^{-9}$ Wm^2/kg. The reason behind these discrepancies is unclear. However, the top boundary energy flux

in Figure 5 is almost exactly the pressure work in Figure 6 as predicted.

4.2 Energy Flux for Single and Double Mixed Layer Profiles

Figure 7 shows the energy flux profiles along with the energy flux through the top and bottom boundaries for the single and double layer stratification profiles shown in Figures 3 and 4. Because the boundary forcing for these simulations is windowed, the energy flux oscillates in time which can be seen in the top panels of 7a and 7b.

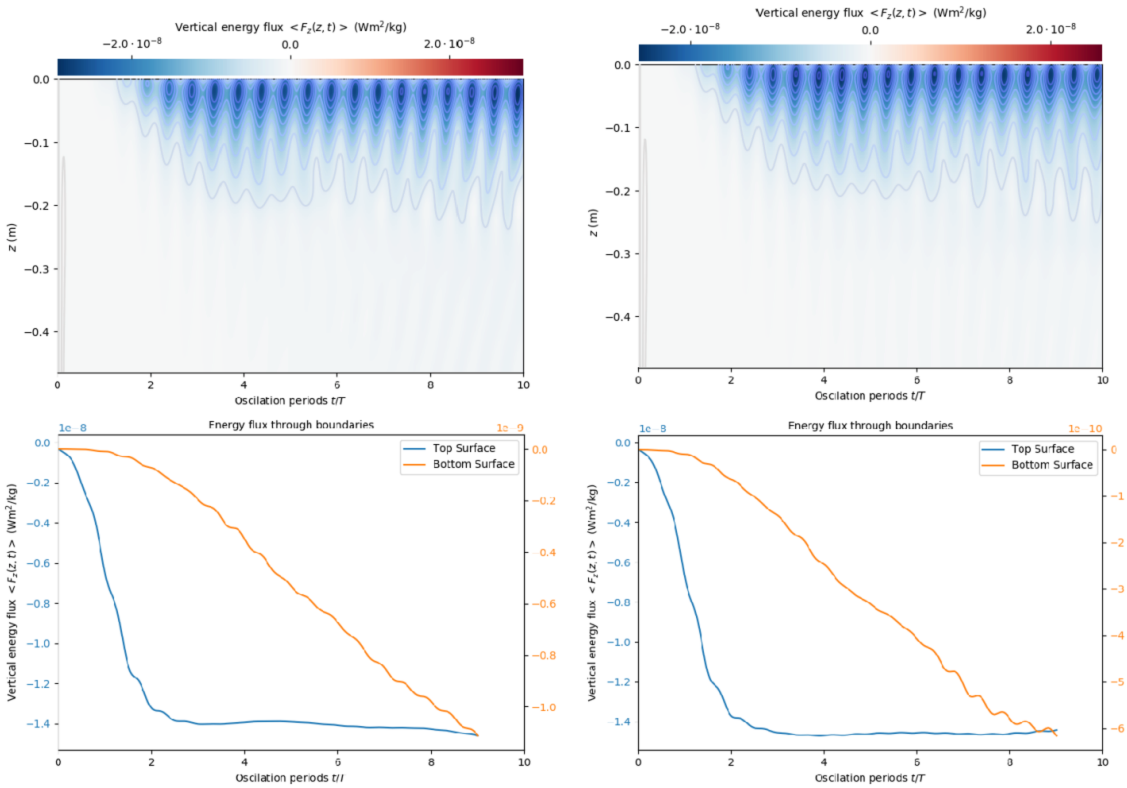

(a) Single layer

(b) Double layer

Figure 7: Energy flux profiles for the single layer (a) and double layer (b) stratification profiles. The bottom panels show the running average over one oscillation period of the vertical energy flux through the top and bottom boundaries. These simulations had $\omega = 0.67$ s^{-1} for (a) or $\omega = 0.71$ s^{-1} for (b), $\hat{A} = 2.3 \cdot 10^{-4}$, and were run for 10 oscillation periods.

To smooth this oscillation, the bottom panels of Figure 7 show the running average over one oscillation period. This is why those plots stop one period before the end of the simulation. The remaining wiggles in the lines would be reduced if the simulations had smaller time steps because that would give more data points per period.

Figure 8 shows plots the running average over one period of the three terms in the en-

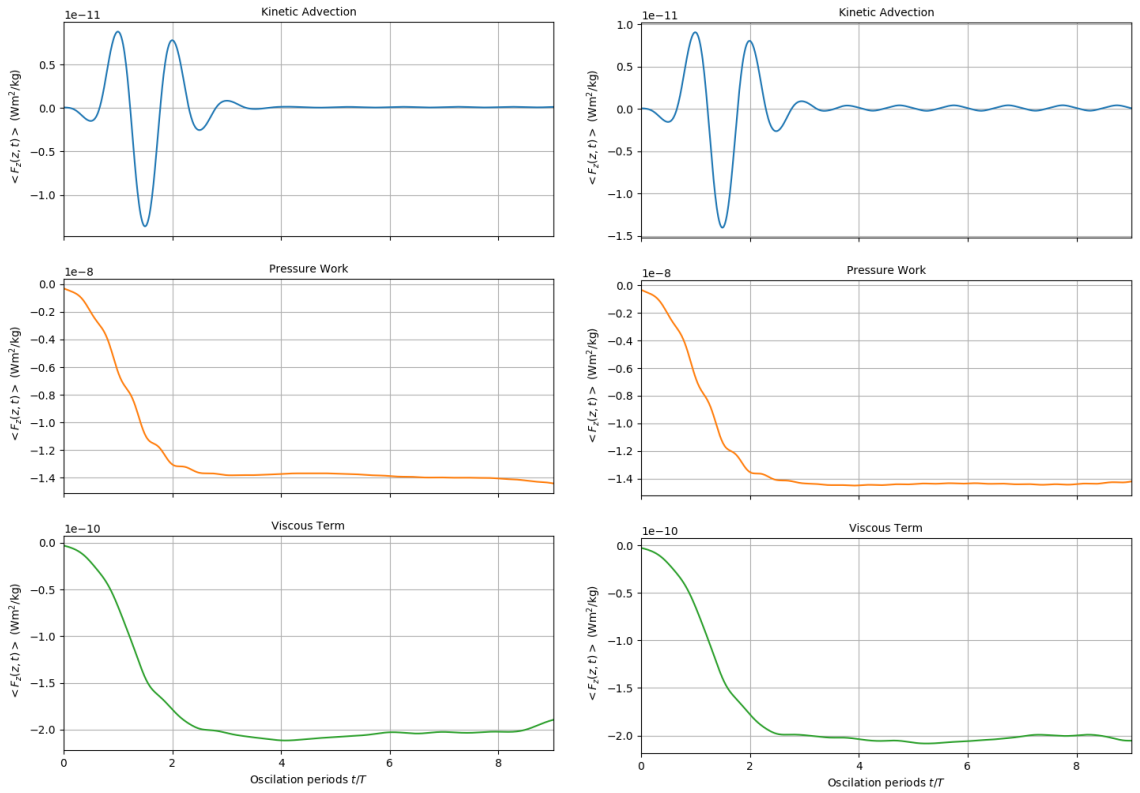

(a) Single layer (b) Double layer

Figure 8: The 3 energy flux terms in (19) on the top boundary for the single layer (a) and double layer (b) stratification profiles. The energy flux values are the running average over one oscillation period. These simulations had $\omega = 0.67$ s^{-1} for (a) or $\omega = 0.71$ s^{-1} for (b), $\hat{A} = 2.3 \cdot 10^{-4}$, and were run for 10 oscillation periods.

ergy flux equation (19) for the top boundaries for the single and double layer stratification profiles shown in Figures 3 and 4. The kinetic advection for both layerings goes to zero as expected. It is unclear why the viscous term does not got to zero as I expect. However, the plots do match the expectation that the pressure works would be almost exactly the same as the total energy fluxes shown in Figure 7.

5 Conclusions

The DNS using spectral methods to solve the Boussinesq equations successfully reproduces the results of laboratory experiments and offers a method of analyzing the vertical propagation of energy through different stratification profiles. While I found that pressure work is indeed the dominant energy flux term as predicted, there are discrepancies between the predicted and simulated energy flux values that need to be resolved.

The code could be improved to reduce aliasing in order to handle waves forced at higher amplitudes. This could be done using HPC resources to increase the spatial and temporal resolution, using an adaptive time stepping procedure, or modifying the implementation of viscosity to increase dissipation. Implementing a sponge layer would further reduce the possibility of waves reflected from the bottom of the domain interfering with the flow of interest.

Future extensions to this project will include adjusting the parameters to be closer to representing the Arctic Ocean as opposed to a laboratory experiment. This will involve reinstating rotational effects, adding more mixed layers to the background stratification profiles, adjusting the diffusivity and viscosity of the fluid, and changing the frequency, amplitude, and windowing of the boundary forced waves. Other extensions would be to make a comparison with the theoretical model presented by Ghaemsaidi et al. (2016) or to use the code to simulate internal wave tunneling through differing numbers and thicknesses of mixed layers.

6 Acknowledgements

I would like to acknowledge my supervisor, Prof. Nicolas Grisouard for invaluable help and guidance throughout this project.

References

Ascher, U. M., Ruuth, S. J., and Spiteri, R. J. (1997). Implicit-explicit Runge-Kutta methods for time-dependent partial differential equations. *Applied Numerical Mathematics*, 25(2-3):151–167.

Burns, K. J., Vasil, G. M., Oishi, J. S., Lecoanet, D., and Brown, B. P. (2019). Dedalus: A Flexible Framework for Numerical Simulations with Spectral Methods. *arXiv e-prints*, page arXiv:1905.10388.

Carmack, E. C. (2007). The alpha/beta ocean distinction: A perspective on freshwater fluxes, convection, nutrients and productivity in high-latitude seas. *Deep-Sea Research Part II: Topical Studies in Oceanography*, 54(23-26):2578–2598.

Carmack, E. C., Aagaard, K., Swift, J. H., Macdonald, R. W., McLaughlin, F. A., Jones, E. P., Perkin, R. G., Smith, J. N., Ellis, K. M., and Killiush, L. R. (1997). Changes in temperature and tracer distributions within the Arctic Ocean: Results from the 1994 Arctic Ocean section. *Deep-Sea Research Part II: Topical Studies in Oceanography*, 44(8):1487–1493.

Comiso, J. C., Parkinson, C. L., Gersten, R., and Stock, L. (2008). Accelerated decline in the Arctic sea ice cover. *Geophysical Research Letters*, 35(1):1–6.

Cushman-Roisin, B. and Beckers, J.-M. (2011). *Introduction to Geophysical Fluid Dynamics. Physical and Numerical Aspects*. Elsevier Ltd.

Fer, I. (2014). Near-Inertial Mixing in the Central Arctic Ocean. *Journal of Physical Oceanography*, 44(8):2031–2049.

Foran, K. (2017). *Modelling Internal Wave Propagation through Layered Fluid Using Spectrally-Based DNS*. Msc thesis, University of Toronto.

Ghaemsaidi, S. J., Dosser, H. V., Rainville, L., and Peacock, T. (2016). The impact of multiple layering on internal wave transmission. *Journal of Fluid Mechanics*, 789:617–629.

Kundu, P. K., Cohen, I. M., and Dowling, D. R. (2015). *Fluid Mechanics*. Academic Press, 6th edition.

Lautrup, B. (2011). *Physics of Continuous Matter: Exotic and Everyday Phenomena in the Macroscopic World*. CRC Press, 2nd edition.

Rainville, L., Lee, C., and Woodgate, R. (2011). Impact of Wind-Driven Mixing in the Arctic Ocean. *Oceanography*, 24(3):136–145.

Rainville, L. and Winsor, P. (2008). Mixing across the Arctic Ocean: Microstructure observations during the Beringia 2005 Expedition. *Geophysical Research Letters*, 35(8):2–6.

Shibley, N. C. and Timmermans, M.-L. (2019). The Formation of Double-Diffusive Layers in a Weakly Turbulent Environment. *Journal of Geophysical Research: Oceans*.

Sutherland, B. R. (2010). *Internal gravity waves*. Cambridge University Press.

Sutherland, B. R. (2016). Internal wave transmission through a thermohaline staircase. *Physical Review Fluids*, 1(1):013701.

Turner, J. (2010). The melting of ice in the arctic ocean: The influence of Double-Diffusive transport of heat from below. *Journal of Physical Oceanography*, 40(1):249–256.

Vallis, G. K. (2017). *Atmospheric and oceanic fluid dynamics: Fundamentals and large-scale circulation, second edition*. Cambridge University Press, 2nd edition.

Wells, M. G. and Wettlaufer, J. S. (2007). The long-term circulation driven by density currents in a two-layer stratified basin. *Journal of Fluid Mechanics*, 572:37–58.

Winters, K. B., MacKinnon, J. A., and Mills, B. (2004). A Spectral Model for Process Studies of Rotating, Density-Stratified Flows. *Journal of Atmospheric and Oceanic Technology*, 21(1):69–94.